Article:
Dunn, E., Robson, A., Young, R.J. et al. (2026) Single atom chemical identification of TMD defects in ambient conditions. Nanotechnology, 37 (13). 135705. ISSN: 0957-4484

https://doi.org/10.1088/1361-6528/ae5194

PAPER • **OPEN ACCESS**

Single atom chemical identification of TMD defects in ambient conditions

To cite this article: E J Dunn *et al* 2026 *Nanotechnology* **37** 135705

Nanotechnology

OPEN ACCESS

RECEIVED
12 October 2025

REVISED
3 February 2026

ACCEPTED FOR PUBLICATION
13 March 2026

PUBLISHED
2 April 2026

PAPER

Single atom chemical identification of TMD defects in ambient conditions

E J Dunn[1,2], **A J Robson**[3], **R J Young**[1] and **S P Jarvis**[1,*]

[1] Physics Department, Lancaster University, Lancaster LA1 4YB, United Kingdom
[2] Mathematical and Physical Sciences, University College London, Gower Street, London WC1E 6BT, United Kingdom
[3] Department of Chemistry, The University of Sheffield, Brook Hill, Sheffield S3 7HF, United Kingdom
[*] Author to whom any correspondence should be addressed.

E-mail: samuel.jarvis@lancaster.ac.uk

Keywords: conductive, AFM, TMD, defect, atomic

Supplementary material for this article is available online

Abstract

The presence of defects in transition metal dichalcogenides (TMDs) can lead to dramatic local changes in their properties which are of interest for a range of technologies including quantum security devices, hydrogen production, and energy storage. It is therefore essential to be able to study these materials in their native environments, including ambient conditions. Here we report single atom resolution imaging of atomic defects in MoS_2, WSe_2 and WS_2 monolayers carried out in ambient conditions using conductive atomic force microscopy (C-AFM). By comparing measurements from a range of TMDs we use C-AFM to identify the most likely atomic species for the defects observed and quantify their prevalence on each material, identifying oxygen chalcogen substitutions and transition metal substitutions as the most likely, and most common, defect types. Moreover, we demonstrate that C-AFM operated in ambient environments can resolve subtle changes in electronic structure with atomic resolution, which we apply to nitrogen-plasma doped WSe_2 monolayers, demonstrating the capability of C-AFM to resolve chemical details via electronic structure at the atomic scale.

1. Introduction

The properties of transition metal dichalcogenides (TMDs) make them promising candidates for improving existing technologies and enabling those of the future [1, 2]. TMDs have a range of interesting properties and applications; some monolayers are direct band-gap semiconductors with excellent optical properties [3], they can be highly catalytic as a result of chalcogen defects introducing active sites [4–6] and, as layered materials, they can be intercalated, allowing the storage of ions in batteries [7], or stacked to form heterostructures with new properties [8]. The disorder introduced by defects can also be harnessed for the creation of security devices [9], exploiting the presence of the unique arrangement of defects in individual TMD flakes which is reflected in the photoluminescence (PL) response [10, 11].

Scanning probe techniques offer a means of direct real-space imaging providing insight into the defects present after fabrication and the processes through which they form and evolve. Recently the ability to resolve these defects with atomic resolution has been demonstrated on TMDs and MXenes using conductive atomic force microscopy (C-AFM) [12, 13] and higher eigenmode techniques [14], complementing the traditional scanning tunnelling microscopy (STM) [15–23].

In this work, the intrinsic defects of mechanically exfoliated TMD monolayers are characterised using C-AFM with atomic resolution in ambient conditions. By comparing results from MoS_2, WSe_2 and WS_2 monolayers, we are able to identify the most likely chemical origins for single atom defects and quantify their prevalence on each material. Moreover, we demonstrate that C-AFM operated in ambient environments can not only resolve defects with atomic resolution, but also detect subtle changes in electronic structure. We apply this method to WSe_2 monolayers intentionally doped through exposure to nitrogen

plasma, where we show that substitutions of individual oxygen and nitrogen atoms on chalcogen sites (O_{Se} and N_{Se}) can be distinguished.

2. Methods

2.1. Sample preparation

To fabricate TMD monolayer samples bulk TMD crystals (MoS_2—Manchester Nanomaterials, WSe_2—HQ Graphene, and WS_2 - 2D Semiconductors) were mechanically exfoliated onto Nitto Blue Tapes (Acrylic/PVC) where repeated exfoliation dispersed and thinned the flakes. The flakes were then exfoliated from the tapes onto pre-prepared PDMS stamps affixed to glass slides where flakes were then assessed for quality using an optical microscope. Few-layer flakes were selected for further study with Raman and PL in a Horiba labRAM instrument using a Laser Quantum 532 nm laser. Spectra were used to identify monolayers which were then transferred using the PDMS dry transfer technique onto a freshly exfoliated highly ordered pyrolytic graphite (HOPG) substrate.

Here we use HOPG which exhibits a near ohmic density of states and can be prepared with large atomically flat terraces [24]. In particular, good electrical contact with HOPG ensures that gap states within the TMD materials can be easily measured with C-AFM.

Plasma treated samples were prepared in a custom-built glass barrelled plasma reactor. The glass barrel of the reactor was a QVF process pipe (De Dietrich, UK) – dimensions 500 mm length, 100 mm diameter, clamped between two custom-made steel end plates which serve as ground electrodes. The system was evacuated using an Edwards RV3 rotary vane pump (base pressure: c. 2×10^{-3} mbar). The pressure within the system was monitored by a Thermovac TTR 96 N SC Pirani gauge and Display One Controller (Leybold UK Ltd) and an in-line liquid nitrogen cold trap was installed to enhance the system base pressure. Plasma was ignited using a RFG-C-100-13 power generator and automatic matching network (Coaxial Power System Ltd, Eastbourne, UK), operated at a frequency of 13.56 MHz, connected to a 1 cm thick copper braid (Tranect Ltd, Liverpool, UK) wrapped around the glass barrel three times. Samples were positioned within the glow region and were electrically floating. A diagram of the plasma chamber is shown in figure S8.

2.2. C-AFM

All scanning probe microscopy (SPM) measurements were collected with a Bruker MultiMode 8 equipped with a Nanoscope V controller. For the flattening of monolayer flakes and removal of contaminants, the AFM was operated in contact mode using NuNano Scout 70 probes ($f_0 \sim 70$ kHz; nominal spring constant 2 Nm^{-1}). Samples were typically then checked in PeakForce mode to ensure no damage to flakes. C-AFM was carried out using Nanoworld CDT-FMR conductive diamond-coated Si probes ($f_0 \sim 105$ kHz; nominal spring constant 6.2 Nm^{-1}). C-AFM measurements were collected by operating in contact mode at a deflection setpoint of 5 nm, corresponding to a force of $\sim$31 nN, typically with a line scan rate of 0.5–1 Hz. A bias voltage was applied to the sample, with the resulting current measured via the conductive probe using a FEMTO DLPCA-200 amplifier.

3. Results

3.1. Flattening of monolayer flakes

Atomic resolution imaging with C-AFM requires atomically flat and electrically conductive substrates, without which features cannot be resolved. Following transfer, the TMD monolayer flakes were flattened using the so-called 'Nano-Squeegee' technique [25]. This process removes the majority of contamination underneath the TMD flakes introduced from the transfer method, greatly improving the electrical contact and creating atomically flat regions of TMD for high-resolution C-AFM measurements. Flattening is achieved by operating the AFM in contact mode at a higher deflection set point and repeatedly scanning the surface, ensuring that the TMD flakes remain undamaged (see figure S1).

3.2. Atomic defects in MoS_2

The formation and structure of atomic defects on MoS_2 is very well studied [12, 17, 20, 22, 23, 26–29], and can be used to aid assignment of the defects observed with C-AFM in other materials. In figure 1 we show the three main defects observed with C-AFM carried out in ambient conditions including images acquired with true atomic resolution.

In figure 1(a) we show the two most common defects observed, identified as either bright or dark features one atom in size. Furthermore, the surrounding nearest neighbour atoms for these defects

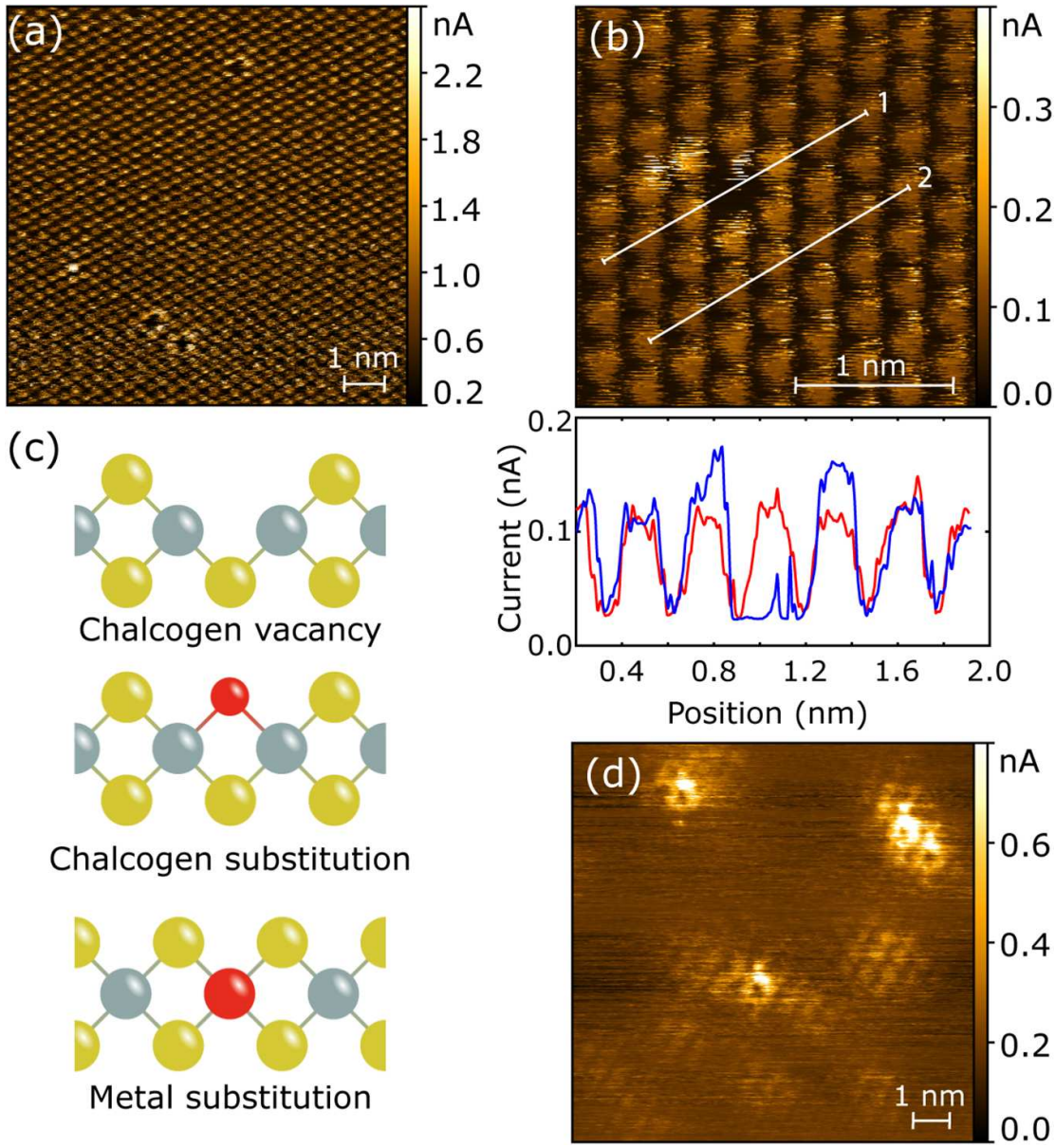

Figure 1. Single atom defects in MoS_2 measured in ambient conditions. (a) C-AFM image showing atomic scale defects visible as either bright or dark features located on sulphur lattice sites. (b) High resolution images show clear augmentation of the measured current in the nearest neighbour sites around individual defects, with line profile analysis indicating an augmentation of almost 50%. (c) Ball-and-stick cartoons depicting the most common defects in MoS_2. (d) C-AFM image showing 'diffuse' defects with large radius. All C-AFM images in this figure were collected on a MoS_2 monolayer on HOPG collected at +0.5 V sample bias.

appear brighter (increased current) compared to the rest of the MoS_2 flake. This is most clearly observed for the dark point defects, as shown in more detail in figure 1(b). The line profile in figure 1(b) reveals that the current signal is almost 50% larger for the nearest neighbour atoms compared to atoms further from the defect, suggesting an increase in local unoccupied states due to the presence of the atomic defect, consistent with previous observations on, and simulations of, TMDs [15, 17, 20, 23, 30]. The precise origin of these single-atom size defects is not universally agreed, with reports suggesting that either sulphur vacancies [12, 13, 17, 26] or oxygen substitutions [15, 22, 31, 32] are responsible. Zhang *et al* [33] suggest that their most common defects are caused by transition metal vacancies because they observe the defect to lie in-between chalcogen sites, but this is inconsistent with our data shown in figure 1. The data from Barja *et al* is particularly compelling, with the combination of STM, dI/dV, and nc-AFM strongly supporting oxygen substitution. Furthermore, the results from Barja *et al* are similar to our own assignment that the bright and dark atomic defects arise from sulphur defects in the bottom and top layers of the MoS_2 monolayer, respectively, with enhancement in the bright defect arising from stronger interaction with the substrate. We also note that whilst our samples are stored

under vacuum, ambient measurements necessitate significant exposure to atmosphere and so atomic vacancies are unlikely. Several studies suggest that oxygen substitutions are energetically favourable [34, 35] and that the presence of a chalcogen vacancy encourages the adsorption and dissociation of molecular oxygen; so that in the presence of oxygen, chalcogen vacancies assist in their own transformation into oxygen substitutions [27, 28, 35]. We note that prior work [36] has shown that whilst defects within the HOPG support can contribute to observed defects in the TMD layer, this effect is not present in pristine untreated HOPG, as also used in our study.

Another less commonly observed defect is shown in figure 1(d). These more diffuse defects appear as either bright (figure 1(d)) or dark (figure S2) features and are characterised by larger lateral dimensions extending over multiple lattice sites. Diffuse defects have previously been observed in C-AFM and attributed to transition-metal substitutions [12, 26]. Defects with 5 nm radius were also imaged by Addou *et al*, using STM on similar samples [17], and Schuler *et al* observed diffuse features arising from charged defects [37].

Charged point defects in TMDs are known to induce local band bending that shifts the conduction- and valence-band edges in opposite directions. As a result, they produce a characteristic bias polarity–dependent contrast: a defect that increases current at positive sample bias will decrease current at negative bias, and vice versa. In our measurements, however, the diffuse defects show the same contrast sign at both positive and negative bias. This can be seen clearly in figures 2(b) and (c), where the same defect in WSe_2 remains depleting from -1 V to $+1$ V. Such polarity-independent behaviour is inconsistent with the expected signature of a charged defect and instead supports an interpretation in terms of neutral transition-metal substitutions, which are known to generate extended LDOS perturbations without reversing contrast between opposite bias polarities. We note that although substrate coupling in C-AFM can influence contrast amplitude, it does not change the fundamental polarity reversal expected for charged centres.

Transition metals can have similar or favourable binding energies when substituted at a molybdenum site when compared to the pristine lattice [38]. Ta, W, Nb, Hf and Zr have higher binding energies than Mo and, as a result, if they are present they could be expected to replace the Mo. We find that diffuse defects are not observed as commonly on MoS_2 as the single atom size defects. This is consistent with the expectation that transition-metal substitutions are relatively rare, occurring only during initial growth of the bulk MoS_2 crystal. These observations therefore support an assignment of diffuse defects to transition metal substitutions, similar to previous reports [12, 26].

3.3. Atomic defects in WSe_2

Beyond MoS_2, two of the most commonly studied 2D-TMDs are WSe_2 and WS_2. There are many STM studies into the chemical nature of defects on WSe_2 and WS_2 in synthetic samples [13, 15, 18, 19, 21, 31, 37, 39, 40]. Here we apply C-AFM as described above in order to identify the frequency and type of atomic vacancy observed in mechanically exfoliated monolayers of each material. Figure 2(a) shows a typical atomic resolution C-AFM image collected on WSe_2 where single atom vacancies are observed. In this case, we observe a much greater number of atomic defects as compared to MoS_2, most of which appear as dark features which are attributed to Se vacancies or O_{Se} substitutions as described in the previous section. The observation of predominantly dark single atom vacancies is consistent across measurements, implying a greater number of defects in the top layer of the WSe_2. We tentatively attribute this to increased atmospheric exposure in the top layer, resulting in a larger number of O_{Se} substitutions.

The increased number of single atom features observed on WSe_2 appears to support reports that defects are more numerous in WSe_2 due to the reduction in air stability for chalcogens with higher atomic numbers [27, 41, 42]. The comparison between MoS_2 and WSe_2 also allows us to provide more insight into the assignment of the atomic defects as oxygen substitutions or chalcogen vacancies. Simulated studies of MoS_2 and WSe_2 reveal similar formation energies for chalcogen vacancies in each material. This is due to an increase in binding energy when changing from Mo to W, which acts to counteract the decrease in binding energy when S is exchanged for Se [27]. Comparatively, the calculated energy barrier for oxygen adsorption onto WSe_2 is much less than that required for MoS_2 [28], suggesting a preference for oxidation on WSe_2. The increased defect density we observe on WSe_2 compared to MoS_2, therefore, suggests that oxidation is most likely responsible, further supporting the assignment of oxygen substitutions rather than Se vacancies.

A higher density of diffuse defects is also observed on WSe_2. As with other samples, diffuse defects are still much less common than site-specific defects; an observation in agreement with Yankowitz *at al.* [19]. A pair of C-AFM images collected at ± 1 V bias show one such defect in figures 2(b) and (c). These defects have a similar lateral size to those on MoS_2 and, similarly, they may be found as both dark or bright features (figure S2); though an individual defect is consistently dark or bright across the voltage

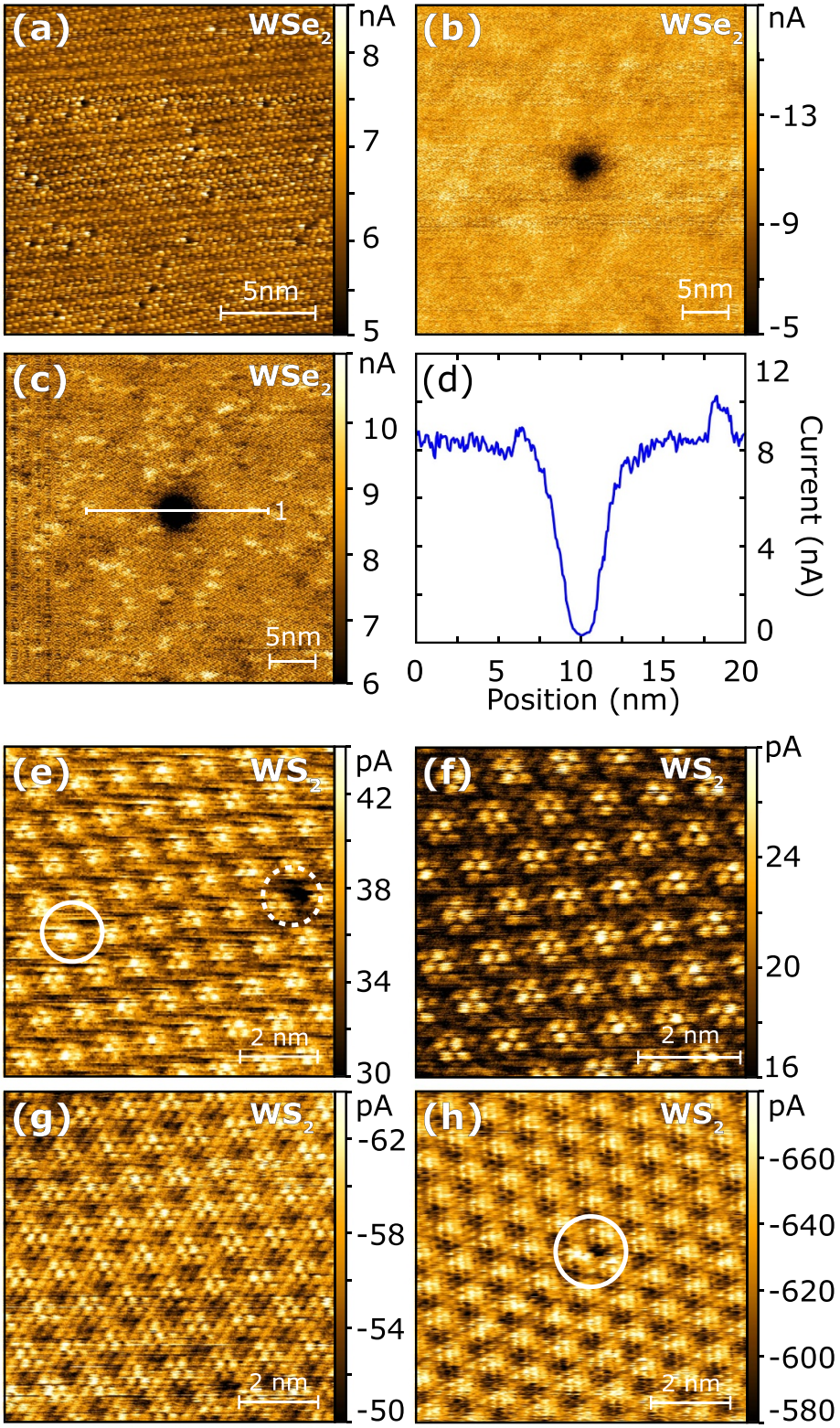

Figure 2. Atomic resolution C-AFM measurements of defects in WSe_2 and WS_2. (a) C-AFM image of atomic depleting defects on a WSe_2 monolayer imaged at 1 V. C-AFM image of a diffuse defect on a WSe_2 monolayer imaged at (b) −1 V and (c) 1 V sample bias. (d) A profile across the diffuse defect indicates a diameter of approximately 5 nm. C-AFM images on WS_2 are dominated by a Moiré pattern from the lattice mismatch with the underlying HOPG. (e) Augmenting (white circle) and depleting (dashed white circle) defects on a WS_2 monolayer observed at 0.5 V sample bias. Images collected at (f) 0.5 V and (g) −1 V sample bias in another region show only the Moiré pattern, with no visible defects. (h) An example of defect, or potentially molecular adsorbate, visible at −0.8 V sample bias.

range used. We note that all C-AFM images presented in this paper use a colour scale that depicts larger current magnitudes as bright, and smaller current magnitudes as dark. It is unclear why some diffuse defects deplete the density of states rather than augment it, though many different transition metals could potentially be substituted into the lattice.

In figure 2(c) which was collected with a sample bias of 1 V we also observe defects with smaller radii. These defects are similar to the single atom size defects observed in other images but appear to be around 1–2 nm in size. We believe this is the result of a slightly blunt tip used in figures 2(b) and (c), as later on in the experiment the resolution improved, allowing us to see these defects.

3.4. Atomic defects in WS_2

Figures 2(e)–(h) shows typical C-AFM images collected on WS_2 monolayers also prepared on HOPG. In this case, strong Moiré patterns between the WS_2 and the HOPG substrate dominate C-AFM images. Repeat measurements suggest that Moiré patterns for WS_2:HOPG are almost ubiquitous, and are very rarely absent. This can be compared to WSe_2:HOPG, where Moiré patterns were also observed, but only at particular bias voltages that could be easily avoided (figure S3).

Despite complications arising from the Moiré patterns, defects are still clearly observed, albeit in much smaller numbers compared to the other TMD materials studied. Figure 2(e)–(h) shows high resolution C-AFM images collected at a range of sample bias voltages between −1 V and 0.5 V. Small site specific defects are highlighted in figure 2(e) showing an augmenting (cyan circle) and depleting defect (red circle) in a C-AFM image collected at 0.5 V sample bias. In this case the Moiré pattern prevents any possibility for atomic resolution, and the defects instead appear to influence a lateral region of ~ 1 nm. Figures 2(g) and (h) shows two images from a separate measurement session with only the Moiré pattern visible collected at 0.5 V and −1.0 V sample bias respectively. A further example of the difficulty in identifying defects can be found in figure 2(h) which shows an example of another site specific defect at −0.8 V sample bias. This defect appears to change lattice site during scanning (slow scan direction is top-to-bottom), showing a 'slice' effect where the defect switches from a dark to a bright feature, laterally offset by around 0.5 nm. This leads to the conclusion that the defect in figure 2(f) may be a surface adsorbate, and so is shown here only for completeness. Diffuse defects, as discussed for WSe_2 and MoS_2, were not observed on WS_2. We tentatively ascribe this to the difficulty in identifying such defects against the background of the Moiré pattern, and, as discussed below, the relatively low density of defects observed on WS_2 compared to the other TMDs studied.

3.5. Quantification of defect densities

In figure 3 WSe_2, MoS_2 and WS_2 are compared side by side. Over a 30 nm by 30 nm area the defect densities are $1.4 \pm 0.1 \times 10^{13}$, $1.6 \pm 0.4 \times 10^{12}$ and $6 \pm 3 \times 10^{11}$ defects per cm^2 for WSe_2, MoS_2 and WS_2 respectively. We note that the calculated density for WS_2 must be considered as a lower estimate due to the Moiré effect described above. The densities of defects observed in figure 3 are consistent with expectations from density functional theory and molecular dynamics studies of oxygen adsorption and dissociation on TMD surfaces and the formation energy of vacancies. Compared to MoS_2, WS_2 should exhibit fewer defects due to an increase in the vacancy formation energy arising from the change of Mo to W [27]; which then, in turn, decreases the adsorption of oxygen onto the surface [35]. Similarly, changing chalcogen from S in WS_2 to Se in WSe_2 increases the vacancy formation energy with the same results. However, it also leads to a higher energy barrier for oxygen adsorption [28].

3.6. Nitrogen doping of WSe_2 Via plasma

The atomic resolution capability of C-AFM, and moreover, the sensitivity to minor changes in conduction, suggests that C-AFM should be capable of identifying variations in local conductance by dopant chemistry. WSe_2 monolayers on HOPG were therefore introduced into a N_2 plasma, creating N_{Se} substitutions that can be compared with the pre-existing O_{Se} discussed above. XPS measurements have previously confirmed that Mo-N bonds can be introduced to MoS_2 through plasma exposure, implying that N_2 plasma creates nitrogen substitutions on the chalcogen sites [29, 43], which have a similar formation energy to O_{Se} [44].

Samples were prepared using a bespoke plasma reactor designed for plasma polymerisation experiments which require cleaner vacuum conditions than a typical plasma oven. The number of N_{Se} substitutions can be carefully controlled by varying gas pressure, power, and the duration of plasma treatment. Using conditions of 10 Pa pressure and 10 W power at 13.56 MHz, we found that 10 s of exposure produced a similar density of N_{Se} defects compared to the pre-existing O_{Se}. Figure 4(a) shows a C-AFM image of single atom O_{Se} depleting defects on WSe_2:HOPG observed before plasma exposure. Following 10 s exposure, a second type of defect appears as shown in figure 4(b), which again appears

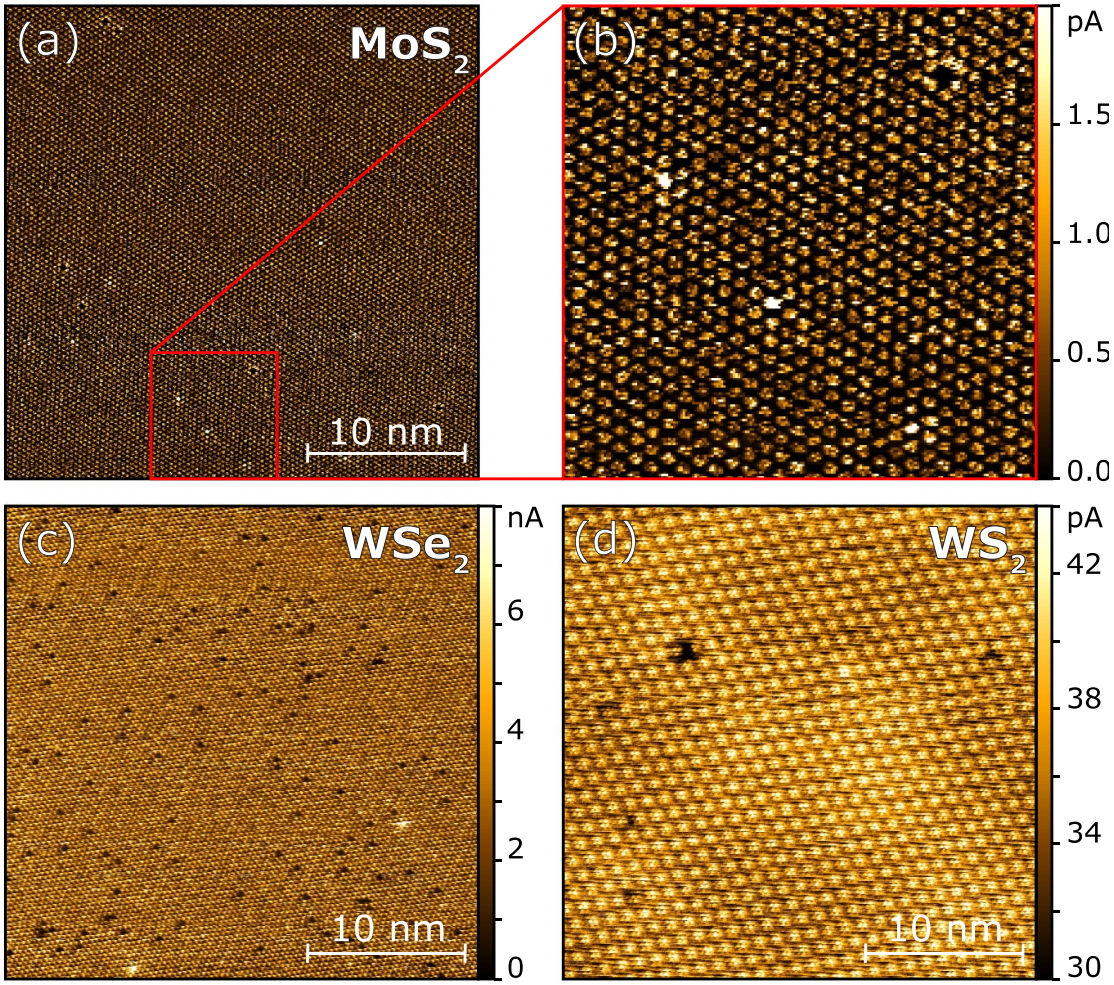

Figure 3. Quantification of defects on MoS_2, WSe_2 and WS_2. 30 nm by 30 nm current channel C-AFM images of site specific defects on (a) MoS_2 collected at 0.5 V sample bias, (c) WSe_2 collected at 1 V sample bias, and (d) WS_2 collected at 0.5 V sample bias. (b) Shows a section of (a) in greater detail. The image on WSe_2 displays the most defects (125), followed by MoS_2 (16) and then WS_2 (6), however the Moiré pattern may hide some of the defects in WS_2. In all three materials a mix of augmenting and depleting defects are observed.

as a single atom depleting site, however, compared to O_{Se}, a faint atomic feature is still visible. These images are taken on the same flake with the same conductive diamond probe, before and after plasma treatment. Profiles taken across the defects are shown in figures 4(e) and (f) alongside enlarged C-AFM images of O_{Se} and the new feature in figures 4(c) and (d), respectively. The line profiles clearly show an increased signal in the depleting region for the new feature compared with O_{Se}, which we find is consistent across samples (and increase in number with greater plasma exposure). In addition, we note that prior to plasma treatment, defects were not frequently observed at nearest-neighbour chalcogen sites, however, in figure 4(b) paired defects are more common and can be observed for both 'faint' and single atom depleting defects. Enlarged examples are shown in figures 4(g)–(h).

It has been reported that nitrogen substitutions should add in-gap states near the valence band [44], however, this does not appear to be reflected in our C-AFM measurements. We postulate this is because unlike O_{Se}, N_{Se} is not iso-electronic, instead acting like a p-type dopant. The underlying HOPG provides access to a carrier reservoir that can fill states, resulting in additional electrons at the dopant site and a local negative charge. As previously discussed, a key signature of a charged defect is asymmetry between negative and positive bias, therefore, at positive bias a negatively charged defect should be observed as a dark feature, which is consistent with the reduction in current characterising the 'faint' defect sites at 1 V. This interpretation, which we infer from the data we have available, is supported by similarities to charged defects observed in STM studies of CVD TMDs with CH_{Se} and CH_S substitutions which are thought to be similar in nature to N_{Se} substitutions [37].

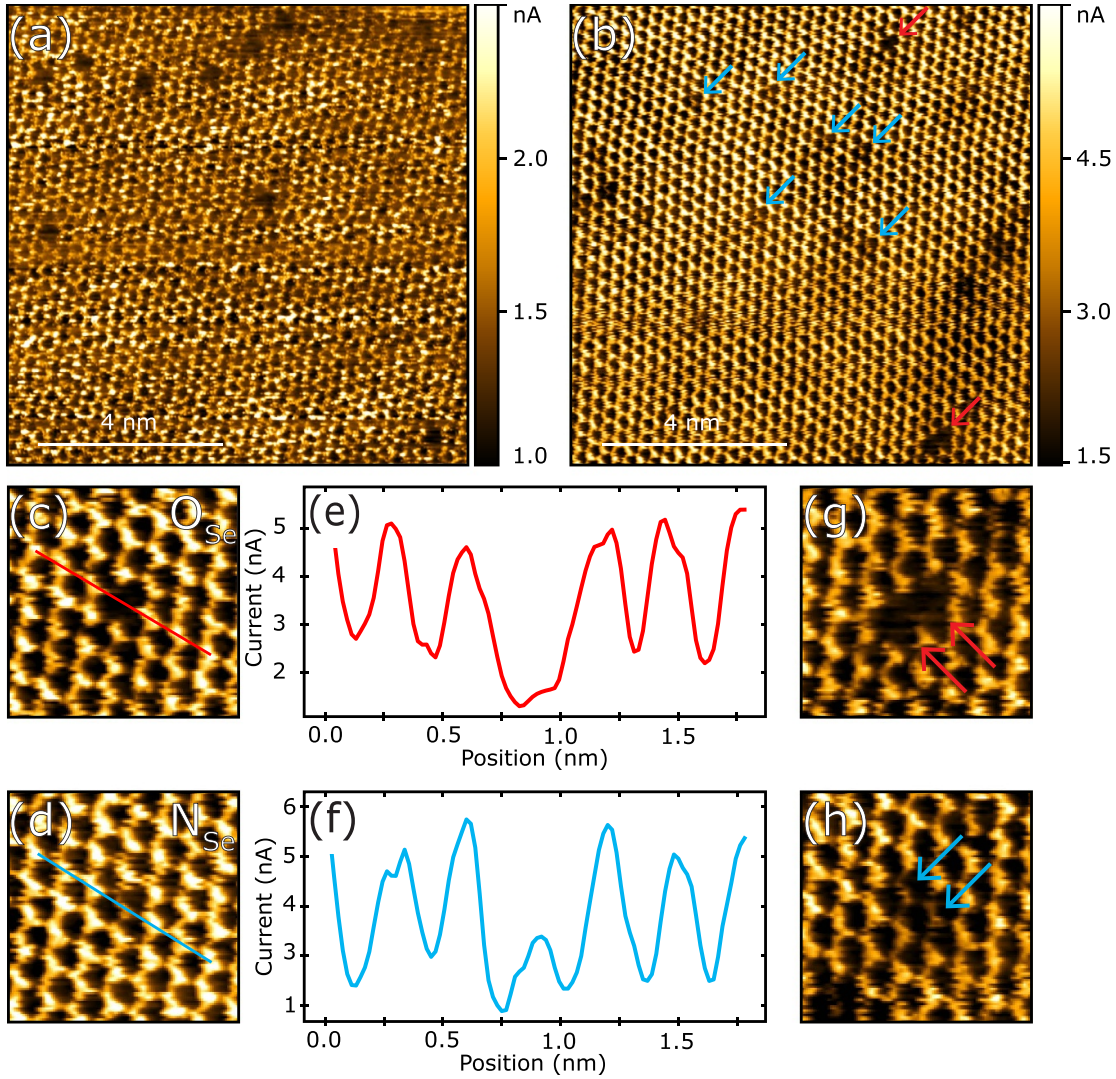

Figure 4. Identification of defects in N_2 plasma treated WSe_2. Current channel C-AFM images of WSe_2 monolayer on HOPG imaged at 1 V (a) before and (b) after plasma exposure. Enlarged C-AFM images show the features which we assign to (c) O_{Se} and (d) N_{Se} in detail, alongside line profiles shown in (e) and (f), respectively. (g) C-AFM image of a pair of O_{Se} defects, compared to (h) a C-AFM image of a pair of N_{Se} defects. Arrows are used throughout the figure to highlight O_{Se} (red) and N_{Se} (blue) features.

3.7. Mechanism of atomic resolution C-AFM in ambient conditions

The diamond-coated probes used in this study last long enough for a full day of measurements, whereas Pt-coated probes could only acquire a small number of images before the conductive signal was lost. Therefore for practical reasons diamond-coated probes were used. Initially, atomic resolution was not expected, however, the diamond probes achieved 'true' atomic resolution in approximately 40% of C-AFM imaging sessions, and lattice resolution reliably achieved over 90% of the time. We note that the probes remained sufficiently sharp for atomic resolution despite a colossal loading force compared to other high resolution imaging techniques [45]. We expect that the high stability of the polycrystalline diamond coating plays an important role in maintaining the sharpness of the tip apex. As discussed above, that atomic resolution is not always achieved and despite the high stability of the diamond probes 'tip changes' are often observed; generally resulting in a change in image quality and potentially atomic resolution. Tip changes are observed as sudden, discontinuous jumps in the current which originate from changes in the nanostructures at the tip apex or from picking up and dropping molecules on the surface. In such cases where atomic resolution is not achieved, we find that the majority of defects appear as bright features around 1–2 nm in size, and we no longer observe a mixture of bright and dark point defects. This appears to be consistent with previous reports on CVD WS_2 using C-AFM with nanoscale resolution [39]. We also note that whilst attempts were made to measure $I(V)$ at specific defect sites, this data was not reliable due to the high thermal drift in ambient conditions.

High-resolution AFM in ambient conditions has been reported by a number of groups [12–14, 26, 46–51] with various proposed imaging mechanisms. On TMD samples both Sumaiya *et al* [12] and Nowakowski *et al* [13] attribute their atomic resolution images to an insulating layer around the tip which is broken in a sufficiently small area as to create a single atom pathway into the tip. Nowakowski *et al* cite studies of the size of the contact area relative to the area of the conducting channel by Enachescu *et al* [52] and Celano *et al* [53]. Enachescu *et al* tentatively propose an insulating layer and Celano *et al* show that the conductive area of the tip is smaller than the contact area when tunnelling through SiO_2 at tip loads from ∼50–150 nN. We note that all of the tip loads used by the reports where true atomic resolution has been realised all lie below this range: ∼2–2.5 nN [13], ∼0 nN [12] and ∼31 nN (this work). We also note that atomic resolution in UHV-AFM experiments using Si probes have been extensively studied [45, 54–57], where it has long been known that a single atom at the tip apex determines the tip-sample interaction [58] (and therefore, what one might consider the tip-sample 'contact' in C-AFM), with no need for insulating layers. We therefore propose that an insulating layer is not necessary to achieve atomic resolution in ambient, and that the diamond probe likely contains nanocrystallites at the tip-apex, which behave in a similar way to the nano-asperities known to facilitate atomic resolution in UHV-AFM experiments. Indeed, the type of diamond-coated probes used in this study have been observed to terminate in nanocrystallites in the 10 nm regime (See figure S4).

4. Conclusions

We have shown that C-AFM is capable of routinely collecting atomic resolution images of a variety of TMD monolayers prepared and measured in ambient conditions. Not only is C-AFM sensitive to single atom defects, but also subtle changes in the local electronic structure including that of nearest neighbour atoms. MoS_2 mechanically exfoliated monolayers on HOPG substrates are used as a well-studied reference where we identify O_S and transition metal substituents as the most likely, and most common defect types. Comparison across MoS_2, WSe_2, and WS_2, monolayers reveal consistent variation in defect density of 1.4×10^{13}, 1.6×10^{12} and 6.7×10^{11} defects per cm^2 for WSe_2, MoS_2 and WS_2 respectively, which correspond well to expected formation energies. Finally, we show that minor variations in electronic structure, which we assign to O_{Se} and N_{Se} substitutions, can be measured in N_2 plasma treated WSe_2:HOPG monolayers further demonstrating the capability of C-AFM to resolve electronic, and therefore infer chemical, details at the atomic scale.

By introducing elements into TMDs intentionally via methods such as the plasma exposure demonstrated here it will be possible to find further evidence to illuminate the chemical origin of the defects observed in this work, identify non-intrinsic defects and establish the impact that these defects have on physical properties of TMDs including the optical emission and catalytic behaviour.

Acknowledgments

S.P.J. thanks the Engineering and Physical Sciences Research Council (EPSRC) and the Royal Society, respectively, for Grants EP/X026876/1 and PI70026. E J D, S P.J, and R J Y gratefully acknowledge funding from the Graphene NOWNANO CDT, EP/L01548X/1. A R and S P J also thank the ERDF for funding via the GISMO project.

Data availability statement

The data that support the findings of this study are openly available at the following URL/DOI: https://doi.org/10.17635/lancaster/researchdata/743 [59].

Supporting Information available at https://doi.org/10.1088/1361-6528/ae5194/data1.

Author contributions

E J Dunn
Data curation (equal), Formal analysis (equal), Methodology (equal), Writing – original draft (equal)

S P Jarvis 0000-0003-4031-1519

Conceptualization (equal), Data curation (equal), Formal analysis (equal), Funding acquisition (lead), Investigation (equal), Methodology (equal), Project administration (lead), Resources (equal), Software (equal), Supervision (lead), Validation (equal), Visualization (equal), Writing – original draft (equal), Writing – review & editing (lead)

References

[1] Manzeli S, Ovchinnikov D, Pasquier D, Yazyev O V and Kis A 2017 2D transmission metal dichalcogenides *Nat. Rev. Mater.* **2** 1–15

[2] Autere A, Jussila H, Dai Y, Wang Y, Lipsanen H and Sun Z 2018 Nonlinear optics with 2D layered materials *Adv. Mater.* **30** 1705963

[3] Mak K F, Lee C, Hone J, Shan J and Heinz T F 2010 Atomically thin MoS 2: a new direct-gap semiconductor *Phys. Rev. Lett.* **105** 136805

[4] Zhu J, Yang R and Zhang G 2022 Atomically thin transition metal dichalcogenides for the hydrogen evolution reaction *Chem. Mater. Phys.* **1** 102–11

[5] Ye G, Gong Y, Lin J, Li B, He Y, Pantelides S T, Zhou W , Vajtai R and Ajayan P M 2016 Defects engineered monolayer MoS_2 for improved hydrogen evolution reaction *Nano Lett.* **16** 1097–103

[6] Wu L and Hofmann J P 2021 Comparing the intrinsic HER activity of transition metal dichalcogenides: pitfalls and suggestions *ACS Energy Lett.* **6** 2619–25

[7] Yun Q, Li L, Hu Z, Lu Q, Chen B and Zhang H 2020 Layered transition metal dichalcogenide-based nanomaterials for electrochemical energy storage *Adv. Mater.* **32** 1903826

[8] Tang B, Che B, Xu M, Ang Z P, Di J, Gao H J, Yang H, Zhou J and Liu Z 2021 Recent advances in synthesis and study of 2D twisted transition metal dichalcogenide bilayers *Small Struct.* **2** 2000153

[9] Cao Y *et al* 2017 Optical identification using imperfections in 2D materials *2D Mater.* **4** 045021

[10] Wu Z *et al* 2016 Defects as a factor limiting carrier mobility in WSe2: a spectroscopic investigation *Nano Res.* **9** 3622–31

[11] Chow P K, Jacobs-Gedrim R B, Gao J, Lu T-M, Yu B, Terrones H and Koratkar N 2015 Defect-induced photoluminescence in monolayer semiconducting transition metal dichalcogenides *ACS Nano* **9** 1520–7

[12] Sumaiya S A, Liu J and Baykara M Z 2022 True atomic-resolution surface imaging and manipulation under ambient conditions via conductive atomic force microscopy *ACS Nano* **16** 20086–93

[13] Nowakowski K, Zandvliet H J W and Bampoulis P 2018 Barrier Inhomogeneities in atomic contacts on WS_2 *Nano Lett.* **19** 1190–6

[14] Severin N, Dzhanoev A R, Lin H, Rauf A, Kirstein S, Palma C-A, Sokolov I M and Rabe J P 2022 Atomic resolution with high-eigenmode tapping mode atomic force microscopy *Phys. Rev. Res.* **4** 023149

[15] Barja S 2019 Identifying substitutional oxygen as a prolific point defect in monolayer transition metal dichalcogenides *Nat. Commun.* **10** 1–8

[16] Chang Y S *et al* 2021 Surface electron accumulation and enhanced hydrogen evolution reaction in $MoSe_2$ basal planes *Nano Energy* **84** 105922

[17] Addou R, Colombo L and Wallace R M 2015 Surface defects on natural MoS_2 *ACS Appl. Mater. Interfaces* **7** 11921–9

[18] Blades W H, Frady N J, Litwin P M, McDonnell S J and Reinke P 2020 Thermally induced defects on WSe_2 *J. Phys. Chem. C.* **124** 15337–46

[19] Yankowitz M, McKenzie D and LeRoy B J 2015 Local spectroscopic characterization of spin and layer polarization in WSe_2 *Phys. Rev. Lett.* **115** 136803

[20] Vancsó P, Magda G Z, Petö J, Noh J-Y, Kim Y-S, Hwang C, Biró L P and Tapasztó L 2016 The intrinsic defect structure of exfoliated MoS_2 single layers revealed by scanning tunneling microscopy *Sci. Rep.* **6** 29726

[21] Zhang C, Wang C, Yang F, Huang J-K, Li L-J, Yao W, Ji W and Shih C-K 2019 Engineering point-defect states in monolayer WSe_2 *ACS Nano* **13** 1595–602

[22] Mitterreiter E, Schuler B, Cochrane K A, Wurstbauer U, Weber-Bargioni A, Kastl C and Holleitner A W 2020 Atomistic positioning of defects in helium ion treated single-layer MoS_2 *Nano Lett.* **20** 4437–44

[23] Petö J, Ollár T, Vancsó P, Popov Z I, Magda G Z, Dobrik G, Hwang C, Sorokin P B and Tapasztó L 2018 Spontaneous doping of the basal plane of MoS2 single layers through oxygen substitution under ambient conditions *Nat. Chem.* **10** 1246–51

[24] Venugopal A, Pirkle A, Wallace R M, Colombo L and Vogel E M 2009 Contact resistance studies of metal on HOPG and graphene stacks *AIP Conf. Proc.* **1173** 324

[25] Rosenberger M R, Chuang H, McCreary K M, Hanbicki A T, Sivaram S V and Jonker B T 2018 Nano-"Squeegee" for the Creation of Clean 2D material interfaces *Appl Mater. Interfaces* **10** 10379–87

[26] Bampoulis P, Van Bremen R, Yao Q, Poelsema B, Zandvliet H J W and Sotthewes K 2017 Defect dominated charge transport and fermi level pinning in MoS_2/metal contacts *ACS Appl. Mater. Interfaces* **9** 19278–86

[27] Liu H, Han N and Zhao J 2015 Atomistic insight into the oxidation of monolayer transition metal dichalcogenides: from structures to electronic properties *RSC Adv.* **5** 17572–81

[28] Longo R C, Addou R, Santosh K C, Noh J-Y, Smyth C M, Barrera D, Zhang C, Hsu Julia W P, Wallace R M and Cho K 2017 Intrinsic air stability mechanisms of two-dimensional transition metal dichalcogenide surfaces: basal versus edge oxidation *2D Mater.* **4** 025050

[29] Azcatl A 2016 Covalent nitrogen doping and compressive strain in MoS2 by remote N2 plasma exposure *Nano Lett.* **16** 5437–43

[30] González C, Biel B and Dappe Y J 2016 Theoretical characterisation of point defects on a MoS_2 monolayer by scanning tunnelling microscopy *Nanotechnology* **27** 105702

[31] Schuler B *et al* 2019 How substitutional point defects in two-dimensional WS_2 induce charge localization, spin–orbit splitting and Strain *ACS Nano* **13** 10520–34

[32] Zheng Y J *et al* 2019 Point defects and localized excitons in 2D WSe_2 *ACS Nano* **13** 6050–9

[33] Zhang S, Wang C-G, Li M-Y, Huang Di, Li L-J, Ji W and Wu S 2017 Defect structure of localized excitons in a WSe_2 monolayer *Phys. Rev. Lett.* **119** 046101

[34] Santosh K, Longo R C, Wallace R M and Cho K 2015 Surface oxidation energetics and kinetics on MoS_2 monolayer *J. Appl. Phys.* **117** 135301
[35] Iordanidou K, Houssa M, Pourtois G, Afanas'ev V V and Stesmans A 2016 Oxygen and hydroxyl adsorption on MS_2 (M = Mo, W, Hf) monolayers: a first-principles molecular dynamics study *Phys. Status Solidi Rapid Res. Lett.* **10** 787–91
[36] Summerfield A 2018 Moiré-modulated conductance of hexagonal boron nitride tunnel barriers *Nano Lett.* **18** 4241–6
[37] Cochrane K A *et al* 2020 Intentional carbon doping reveals CH as an abundant charged impurity in nominally undoped synthetic WS_2 and WSe_2 *2D Mater.* **7** 031003
[38] Cheng Y C, Zhu Z Y, Mi W B, Guo Z B and Schwingenschlögl U 2013 Prediction of two-dimensional diluted magnetic semiconductors: doped monolayer MoS2 systems *Phys. Rev. B* **87** 100401
[39] Rosenberger M R, Chuang H J, McCreary K M, Li C H and Jonker B T 2018 Electrical characterization of discrete defects and impact of defect density on photoluminescence in monolayer WS_2 *ACS Nano* **12** 1793–800
[40] Aghajanian M, Schuler B, Cochrane K A, Lee J-H, Kastl C, Neaton J B, Weber-Bargioni A, Mostofi A A and Lischner J 2020 Resonant and bound states of charged defects in two-dimensional semiconductors *Phys. Rev. B* **101** 081201
[41] Mirabelli G, McGeough C, Schmidt M, McCarthy E K, Monaghan S and Povey I M 2016 Air sensitivity of MoS_2, $MoSe_2$, $MoTe_2$, HfS_2 and $HfSe_2$ *J. Appl. Phys.* **120** 125102
[42] Ye F, Lee J, Hu J, Mao Z, Wei J and Feng P X L 2016 Environmental instability and degradation of single- and few-layer WTe2 Nanosheets in ambient conditions *Small* **12** 5802–8
[43] Su T H and Lin Y J 2016 Effects of nitrogen plasma treatment on the electrical property and band structure of few-layer MoS2 *Appl. Phys. Lett.* **108** 033103
[44] Komsa H P, Kotakoski J, Kurasch S, Lehtinen O, Kaiser U and Krasheninnikov A V 2012 Two-dimensional transition metal dichalcogenides under electron irradiation: defect production and doping *Phys. Rev. Lett.* **109** 035503
[45] Yurtsever A, ández Torre D F, González C, Jelínek P, Pou P, Sugimoto Y, Abe M, Pérez R and Morita S 2012 Understanding image contrast formation in TiO_2 with force spectroscopy *Phys. Rev. B* **85** 125416
[46] Wastl D S, Weymouth J and Giessibl F J 2013 Optimizing atomic resolution of force microscopy in ambient conditions *Phys. Rev. B* **87** 245415
[47] Wastl D S, Michael J, Weymouth J and Giessibl F J 2015 Atomic resolution of calcium and oxygen sublattices of calcite in ambient conditions by atomic force microscopy using qplus sensors with sapphire tips *ACS Nano* **9** 3858–65
[48] Schimmel T, Koch T, Küppers J and Lux-Steiner M 1999 True atomic resolution under ambient conditions obtained by atomic force microscopy in the contact mode *Appl. Phys. A* **68** 399–402
[49] Korolkov V V, Summerfield A, Murphy A, Amabilino D B, Watanabe K, Taniguchi T and Beton P H 2019 Ultra-high resolution imaging of thin films and single strands of polythiophene using atomic force microscopy *Nat. Commun.* **10** 1537
[50] Korolkov V V, Timokhin I G, Haubrichs R, Smith E F, Yang L, Yang S, Champness N R, Schröder M and Beton P H 2017 Supramolecular networks stabilise and functionalise black phosphorus *Nat. Commun.* **8** 1385
[51] Bradford J, Cheng T S, James T S S, Khlobystov A N, Mellor C J, Watanabe K, Taniguchi T, Novikov S V and Beton P H 2023 Graphene nanoribbons with hBN passivated edges grown by high-temperature molecular beam epitaxy *2D Mater.* **10** 035035
[52] Enachescu M, Schleef D, Ogletree D F and Salmeron M 1999 Integration of point-contact microscopy and atomic-force microscopy: application to characterization of graphite/Pt(111) *Phys. Rev. B* **60** 16913
[53] Celano U, Hantschel T, Giammaria G, Chintala R C, Conard T, Bender H and Vandervorst W 2015 Evaluation of the electrical contact area in contact-mode scanning probe microscopy *J. Appl. Phys.* **117** 214305
[54] Custance O, Perez R and Morita S 2009 Atomic force microscopy as a tool for atom manipulation *Nat. Nanotechnol.* **4** 803–10
[55] Pou P, Ghasemi S A, Jelinek P, Lenosky T, Goedecker S and Perez R 2009 Structure and stability of semiconductor tip apexes for atomic force microscopy *Nanotechnology* **20** 264015
[56] Jarvis S P, Kantorovich L and Moriarty P 2013 Structural development and energy dissipation in simulated silicon apices *Beilstein J. Nanotechnol.* **4** 941–8
[57] Sweetman A, Stirling J, Jarvis S P, Rahe P and Moriarty P 2016 Measuring the reactivity of a silicon-terminated probe *Phys. Rev. B* **94** 115440
[58] Giessibl F J 1992 Theory for an electrostatic imaging mechanism allowing atomic resolution of ionic crystals by atomic force microscopy *Phys. Rev. B* **45** 13815
[59] Dunn E J, Robson A J, Young R J and Jarvis S P 2026 Data for single atom chemical identification of TMD defects in ambient conditions *Lancaster University* (https://doi.org/10.17635/lancaster/researchdata/743)